

*MR-guided attenuation map for prostate
PET-MRI: an intensity and morphologic-
based segmentation approach for
generating a five-class attenuation map in
pelvic region*

**M. Shirin Shandiz, H. Saligheh Rad,
P. Ghafarian, M. Bakhshayesh Karam,
Afshin Akbarzadeh & Mohammad Reza
Ay**

Annals of Nuclear Medicine

ISSN 0914-7187

Ann Nucl Med

DOI 10.1007/s12149-016-1128-1



Your article is protected by copyright and all rights are held exclusively by The Japanese Society of Nuclear Medicine. This e-offprint is for personal use only and shall not be self-archived in electronic repositories. If you wish to self-archive your article, please use the accepted manuscript version for posting on your own website. You may further deposit the accepted manuscript version in any repository, provided it is only made publicly available 12 months after official publication or later and provided acknowledgement is given to the original source of publication and a link is inserted to the published article on Springer's website. The link must be accompanied by the following text: "The final publication is available at link.springer.com".

MR-guided attenuation map for prostate PET-MRI: an intensity and morphologic-based segmentation approach for generating a five-class attenuation map in pelvic region

M. Shirin Shandiz^{1,2} · H. Saligheh Rad^{1,2} · P. Ghafarian^{3,4} · M. Bakhshayesh Karam^{3,4} · Afshin Akbarzadeh² · Mohammad Reza Ay^{1,2}

Received: 12 May 2016 / Accepted: 13 September 2016
© The Japanese Society of Nuclear Medicine 2016

Abstract

Purpose Prostate imaging is one of the major application of hybrid PET/MRI systems. Inaccurate attenuation maps (μ -maps) derived by direct segmentation (SEG) in which the cortical bone is ignored and the volume of the air in cavities is underestimated is the main challenge of commercial PET/MRI systems for the quantitative analysis of the pelvic region. The present study considered the cortical bone and air cavity along with soft tissue, fat, and background air in the μ -map of the pelvic region using a method based on SEG. The proposed method uses a dedicated imaging technique that increases the contrast between regions and a hybrid segmentation method to classify MR images based on intensity and morphologic characteristics of tissues, such as symmetry and similarity of bony structures.

Procedures Ten healthy volunteers underwent MRI and ultra-low dose CT imaging. The dedicated MR imaging technique uses the short echo time (STE) based on the conventional sequencing implemented on a clinical 1.5T MRI scanner. The generation of a μ -map comprises the

following steps: (1) bias field correction; (2) hybrid segmentation (HSEG), including segmenting images into clusters of cortical bone-air, soft tissue, and fat using spatial fuzzy c-means (SFCM), and separation of cortical bone and internal air cavities using morphologic characteristics; (3) the active contour approach for the separation of background air; and (4) the generation of a five-class μ -map for cortical bone, internal air cavity, soft tissue, fat tissue, and background air. Validation was done by comparison with segmented CT images.

Results The Dice and sensitivity metrics of cortical bone structures and internal air cavities were 72 ± 11 and 66 ± 13 and 73 ± 10 and 68 ± 20 %, respectively. High correlation was observed between CT and HSEG-based μ -maps ($R^2 > 0.99$) and the corresponding sinograms ($R^2 > 0.98$).

Conclusions Currently, pelvis μ -maps provided by the current PET/MRI systems and the ultra-short echo time and atlas-based methods tend to be inaccurate. The proposed method acceptably generated a five-class μ -map using only one image.

Keywords PET/MRI · MRI-base attenuation correction · STE pulse sequence · Morphologic characteristics-based segmentation · Prostate imaging

✉ Mohammad Reza Ay
mohammadreza_ay@tums.ac.ir

¹ Department of Medical Physics and Biomedical Engineering, Tehran University of Medical Sciences, Tehran, Iran

² Research Center for Molecular and Cellular Imaging, Tehran University of Medical Sciences, Tehran, Iran

³ Chronic Respiratory Diseases Research Center, National Research Institute of Tuberculosis and Lung Diseases (NRITLD), Shahid Beheshti University of Medical Sciences, Tehran, Iran

⁴ PET/CT and Cyclotron Center, Masih Daneshvari Hospital, Shahid Beheshti University of Medical Sciences, Tehran, Iran

Introduction

The use of the hybrid PET/MRI in research and clinics has expanded owing to its potential for major breakthroughs in imaging and therapy and developments in its technology [1, 2]. The integrated PET/MRI developed for simultaneous PET and MRI imaging is a unique technology in this context [1, 2]. Using this technology, the mis-overlay

between the two imaging modalities is better minimized in PET/MRI scanners than in PET/CT and SPECT/CT scanners [2]. The main advantage of PET/MRI over PET/CT stems from the use of MRI pulse sequence to increase the contrast in soft tissue, sensitivity during detection of bone metastases, and information about lesions [3]. The decrease in the absorbed dose, a critical issue for ionizing radiation-based imaging and patient follow-up, is another advantage of PET/MRI relative to PET/CT [2]. These benefits improve the depiction and analysis of challenging anatomic parts, such as the pelvis and prostate [3]. Despite these advantages and the promising preliminary clinical results, MRI-guided attenuation correction (MRAC) remains a main concern in PET/MRI, because it lacks an accurate and reliable strategy [4].

In MRI, the signal depends on the proton density and the relaxation times (T1 and T2) of the biological tissues, while the CT data depend on the electron density correlating with the attenuation coefficients of tissues for photons of 511 keV. Given that the MRI signal is not directly associated with electron density, there is no correlation between the MRI signal and the attenuation coefficients of biological tissues. Despite the large difference between the attenuation coefficient of the air and bone at 511 keV, they have similar intensities in MR images. This means that the accurate and simple strategy used in PET/CT for the generation of μ -maps cannot be employed in hybrid PET/MRI systems.

Of the proposed MRAC strategies [4–8], the two most important are the atlas (AT) [7] and direct segmentation (SEG) [5, 6]. AT-based approaches rely on a reference atlas constructed using many CT/MR image pairs. To generate an attenuation map (μ -map), an atlas is registered on the MR images [7]. SEG-based approaches segment the image directly into several tissue classes. These approaches have reproducible results and are general, robust, and fast [9]. Commercial PET/MRI scanners use these methods for MRAC [5, 6, 9]. A three-class μ -map (background air, lung, and soft tissue) has been implemented on a Philips Ingenuity TF PET/MR which is an adaptation of Schulz's approach [6]. A four/five-class μ -map (background air, lung, fat, mixture of fat and water, and water) was implemented using a Siemens mMR PET/MR as an adaptation of the Martínez–Moller approach [5]; however, the SEG-based μ -maps suffer from the lack of high accuracy caused by partial volume effect and ignoring bones [5, 6].

The AC strategy used on commercial PET/MRI systems yields satisfactory outcomes in a whole-body PET/MRI, ignores bone regions, and underestimates air cavity volume, which has a noticeable effect on SUV estimation in some regions [10–12]. These regions include the pelvis with the prostate which has thick cortical bones and air cavities. Because organs, such as the prostate, are a primary application of PET/MRI imaging, improvements in

AC are necessary [3]. The ultra-short echo time (UTE) sequences can detect the signals of the cortical bone and has been introduced for MRAC. The initial results on the application of UTE-based AC on the head are promising [13], but this technique requires development for use in organs with large fields of view (FOV), such as the pelvis [14]. UTE sequences often generate progressive artifacts with an increase in FOV that hampers bone visualization [14, 15]. UTE sequencing is also relatively time-consuming, requiring several minutes per bed position, which could lead to motion artifacts [14].

Brain ACs based on AT are reliable and robust because of the rigidity of the head region. The application of this strategy for the whole-body, however, is not feasible, because registration in AT is error prone in non-rigid regions, such as the thorax and pelvis. Because a pure AT approach is knowledge-guided, its performance is limited to anatomies that are similar to those stored in the corresponding atlas [9, 14]. As a result, it likely to fail to cover patients having anatomical variations and moveable air cavities in the pelvis [14]. Although the AT/pattern recognition (AT/PR) introduced by Hofmann et al. [7] performs better than pure AT, its behavior in challenging regions, such as the pelvis, is unclear and requires further assessment [16].

The present study developed and evaluated a simple, patient-based (not knowledge-based), fully automated technique to segment MR images and generates a more accurate μ -map for pelvic organs. The proposed technique (HSEG) takes the advantage of the SEG approach employed in the current commercial PET/MRI systems and uses the following morphological characteristics of bony structures: symmetry, similarity, area, and perimeter. The proposed technique segments dedicated MR images into five classes: cortical bone, background air, internal air, fat, and soft tissue. These images are achieved using only one scan. The accuracy of the HSEG approach was compared with the CT using the sensitivity, Dice, Jaccard, Hausdorff distance (HD), relative volume error (RVE), and joint histogram approaches.

Materials and methods

Image acquisition

MR imaging of the pelvic region was performed using a 1.5 T MRI system (Magnetom Avanto; Siemens Medical Solutions; Germany). The STE sequence proposed by Khateri et al. [17] was used to increase contrast between regions and segmentation performance. It was shown empirically that segmentation performance using STE was better than the 3D multi-stack spoiled T1-weighted

gradient and 3D T1-weighted turbo spin echo. STE is based on the gradient echo sequence (GRE) sequence applied to the pelvic organs of ten healthy volunteers using the following parameters: TE 1.31 ms, TR 20 ms, FA 15°, BW 501 Hz/pixel, NEX of 1, and total acquisition time of 4.39 min. A total of 600 slices (60 slices in each data set) having a voxel size of $0.99 \times 0.99 \times 4 \text{ mm}^3$ were used.

Ultra-low dose CT imaging was applied using a Light-Speed VCT 64 CT scanner (GE Healthcare Technologies; USA) to generate CT-based μ -maps. The CT protocol of 120 kVp and 10 mAs and a voxel size of $0.79 \times 0.79 \times 3.75 \text{ mm}^3$ were used. This protocol was approved by the ethical committee of the Tehran University of Medical Sciences (license number 1432) and all patients signed informed consent forms.

In MRI and CT scans, the subjects were positioned supine with hands on chest. The superior and inferior limits were set by scout view that those were from the iliac crests to inferior to the lesser trochanter, respectively, in both imaging. In addition, adjusting subject position in middle of FOV was performed by scout view. Each subject was set up by the same technician in both the scans to ensure the most similar positioning. To decrease registration error, the CT scan was performed within 5 min of the MRI. Furthermore, a carbon fiber base plate was located on the CT couch to increase the similarity of body position in MRI and CT scans. This base plate is used for registration procedure in clinic (radiotherapy).

MR image processing

All image processing steps except registration were implemented in MATLAB. Figure 1a shows the steps employed to generate a five-class MRI-based μ -map.

MRI inhomogeneity correction

MRI inhomogeneity (bias field) is commonly caused by object-dependent interactions and imperfections in radiofrequency coils [18]. The correction of inhomogeneity is necessary for MRI segmentation, particularly in regions with a large FOV, such as the pelvis. The automatic-non-parametric approach proposed by Manjoun et al. [18] was used in which inhomogeneity is modeled using spline-based basis functions. The coefficients related to these functions were locally calculated using MR data by minimizing the intensity-gradient entropy-related cost function [18].

MRI segmentation

HSEG was performed slice-by-slice (2D) as described in the following.

Image clustering

The inhomogeneity-corrected images were automatically clustered into bone-air, soft tissue, and fat classes (Fig. 1a) using the spatial fuzzy c-means (SFCM) approach. In contrast to the FCM method, this approach incorporates global local spatial information in the image to reduce mis-clustering and spurious blobs, especially in noisy images, such as STE [19].

Separating cortical bone and internal air structures

Because bone and internal air structures have similar intensities in MR images, they were classified in the same cluster by SFCM, as shown in Fig. 1. A simple and fast algorithm was developed in MATLAB to separate them utilizing the morphologic characteristics of symmetry, similarity, area, and perimeter. The main steps of this algorithm are as follows:

- Step 1 After converting the bone-air cluster in each slice to a binary image, the boundaries of the objects were automatically traced and labeled (Fig. 1a), and the area and perimeter were determined
- Step 2 Since subject position was adjusted in the middle of FOV during scout view imaging, the symmetry axis was located on the midline of the body. In this situation, bony structures, such as the pelvis, are somewhat symmetric pairwise (Fig. 1); thus, this morphologic characteristic was used to distinguish bony objects from massive air objects. To find the symmetric counterpart (doublet) of a bony object, such as b_1 , in Fig. 1b, this object was flipped in the left/right directions (b_1' in Fig. 1b) around a symmetry axis. The number of overlapping pixels between the object and the other objects in the slice was then calculated. This process was repeated for each object in the slice. Normally, only perfectly (or partially) symmetric pairwise bones have some overlapping pixels
- Step 3 Figure 1b shows that bony objects b_1' and b_2 are similar in shape and size. This feature was used to improve object separation in the previous step using the 2D cross-correlation ($C(i, j)$) index [20]. Because this index is invariant with regard to the position of the objects, the two similar objects located in each position can be recognized regardless of the presence or absence of symmetry [20]. The equation of this index is as follows:

$$C_{A_{o_1}-A_{o_2}}(i, j) = \sum_{m=0}^{M_1-1} \sum_{n=0}^{N_1-1} A_{o_2}^f(m, n) \cdot \text{conj}(A_{o_1}(m + i, n + j)) \quad (1)$$

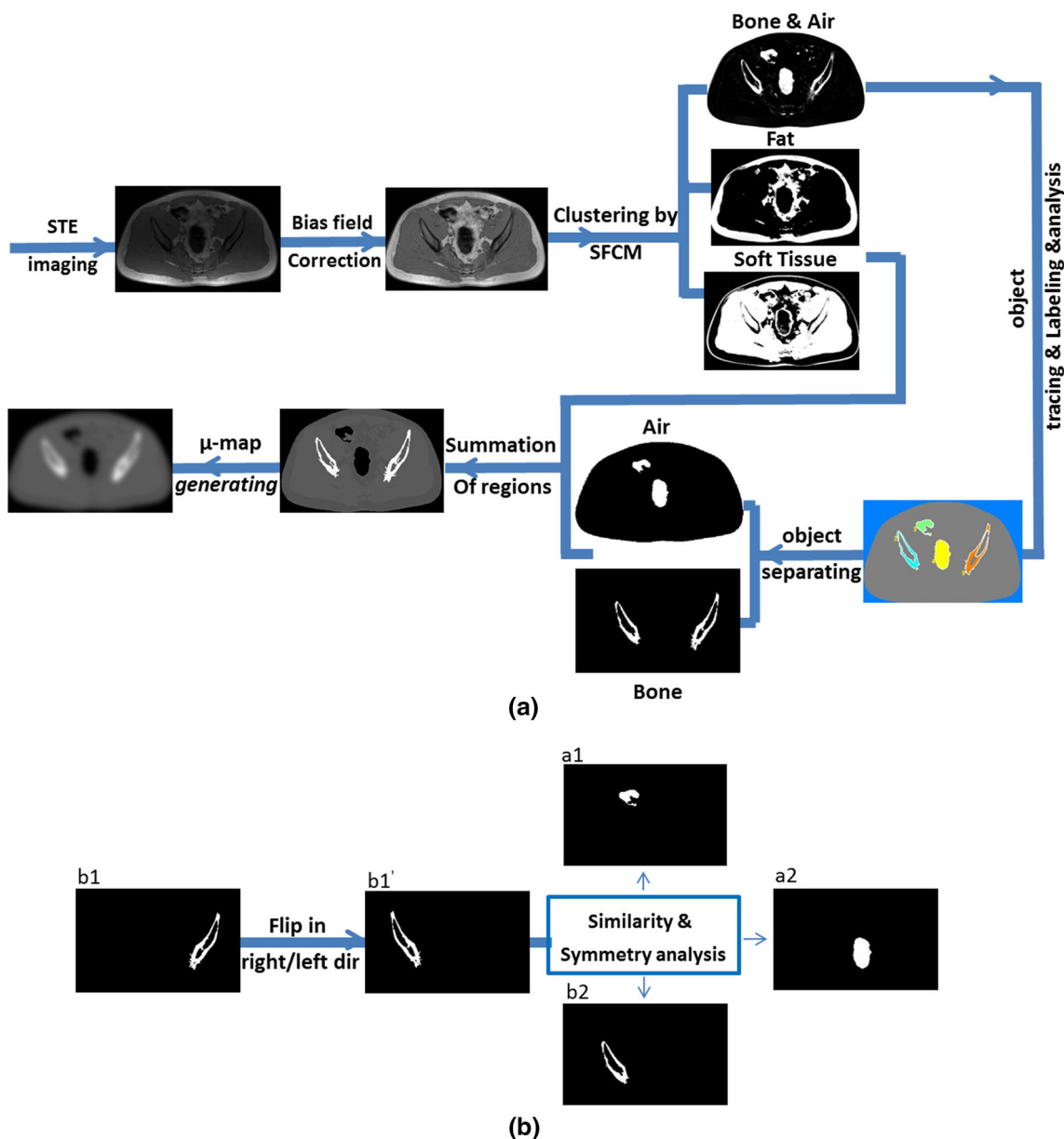


Fig. 1 **a** Workflow of the hybrid algorithm proposed for segmenting and generating a five-class μ map. **b** Object separation based on symmetry and similarity features of bony structures

$$SV_{A_{o1}_A_{o2}} = \text{Max}(C_{A_{o1}_A_{o2}}(i,j)) \tag{2}$$

where $0 \leq i < M_1 + M_2 - 1$ and $0 \leq j < N_1 + N_2 - 1$, as well as $M_1 \times N_1$ and $M_2 \times N_2$ are the matrix size of objects A_{o1} and A_{o2}^f , respectively. A_{o2}^f and $SV_{A_{o1}_A_{o2}}$ denote the flipped matrix of object A_{o2} and the similarity value between two objects, respectively. conj operator returns complex conjugate of the element of A_{o1} , which is not effective on our images owing to the fact that all pixel intensities were real numbers.

Two objects with similar areas and perimeters may have some overlapping pixels (more than 10 pixels), and the peak of SV is considered to be bone in each slice. Because massive air

cavities do not simultaneously possess all features mentioned, these can be separated from the bony regions.

A closing morphologic operation was applied on bone masks for connecting the area of discontinuities [21], followed by a dilating morphologic operation to bold cortical bone structures, because these are depicted smaller than their actual size in STE images [22].

Background segmentation

The Chan–Vese method was used to segment the background (external air) of pelvic MR images. A circular

initial contour was defined at the center of the image over 300 iterations to capture the border of the body and separate it from the background [23].

MR-based μ -map generation

The binary masks of the cortical bone, internal air cavity, background, soft tissue, and fat were added into a zero 3D matrix (Fig. 1a). Then, a kernel of 3×3 was applied in z direction on the matrix for connecting the object contours smoothly along slices. The attenuation coefficients of the tissues at 511 keV were assigned to each mask according to the values in ICRU 44 [24]. The assigned values were 0.172, 0.000, 0.000, 0.096, and 0.089 cm^{-1} for cortical bone, internal air cavity, background, soft tissue, and fat, respectively [5, 11]. To generate a typical μ -map, the segmented images were down-sampled to a matrix size of 256×256 and smoothed by a Gaussian filter with 5 mm full-width at half-maximum (FWHM) to be matched with the spatial resolution of the PET images.

CT data processing

To assess the validity of HSEG for segmentation of MR images, the corresponding CT data was utilized as a reference. The 3D CT images were registered on 3D MR images after pre-processing, which was necessary for acceptable registration. The main pre-registration steps were couch and background removal, as well as image denoising. The first two steps were performed using the Chan–Vese approach [23]. For CT denoising, the non-local mean introduced by Mairal et al. was employed [25].

Image registration

The 3D registration was performed using the Elastix package as based on the insight segmentation and registration toolkit [26]. Because pelvic region is a non-rigid region [27], two-step registration was applied to CT images to achieve close to perfect alignment between the CT and MR data as described previously [27]. The steps are as follows:

Step 1 The CT images underwent an affine transformation using the following parameters: number of histogram bins = 32, number of resolutions = 4, and maximum number of iterations at each resolution level = 250. The optimizer and metric used were adaptive stochastic gradient descent and advanced mutual information, respectively

Step 2 The transformed CT images underwent non-rigid alignment using b-spline transformation on the parameters used in the previous section, except that the maximum number of iterations was 2000 [27]. The performance of registration results was assessed using Dice and Jaccard metrics that measure the mean and union overlap, respectively, between the CT and MR labeled regions [27]

CT segmentation and μ -map generation

The deformed CT images were segmented by thresholding into cortical bone ($I > 300$ HU), soft tissue ($20\text{HU} < I < 300$ HU), fat tissue ($-100 \text{HU} < I < 20$ HU), internal air ($I < -100$ HU), and background ($I < -100$ HU) [5, 11]. The same attenuation coefficients used in MR-based μ -map generation were assigned to each class to evaluate HSEG. The segmented images were then down-sampled to a matrix 256×256 in size and smoothed using a Gaussian filter with an FWHM of 5 mm.

Quantitative assessment

Of the 60 MR slices in each data set, 54 were employed for quantitative assessment and the rest (the first and the final three slices) were omitted owing to noticeable registration errors. To evaluate the HSEG segmentation method, the sensitivity, Dice, and Jaccard metrics, which compare the similarity of segmentation results via measuring the percentage volume overlap between them, were calculated. These metrics were calculated by voxel-by-voxel comparison between CT-based and MR-based binary masks as

$$\text{Sensitivity } (CT_r, MR_r) = \frac{|CT_r \cap MR_r|}{|CT_r|} \times 100 \quad (3)$$

$$\text{Dice } (CT_r, MR_r) = \frac{2|CT_r \cap MR_r|}{|CT_r| + |MR_r|} \times 100 \quad (4)$$

$$\text{Jaccard } (CT_r, MR_r) = \frac{|CT_r \cap MR_r|}{|CT_r \cup MR_r|} \times 100 \quad (5)$$

where CT_r and MR_r are the binary segmented regions (cortical bone, soft tissue, fat, and air cavity) from the reference CT images and MR images, respectively, and the “absolute value” sign means the number of all voxels which meet the set operator conditions in the relation.

As such, the RVE measuring volume overlay error was computed using Eq. (6). This index accurately compared similar masks in the CT and MRI images regardless of the presence of mis-registration error as a confounder [27]:

$$\text{Relative volume error(RVE)} = \frac{|\text{MR}_r| - |\text{CT}_r|}{|\text{CT}_r|} \times 100. \quad (6)$$

The HD was calculated using Eq. (7). This index as a surface distance measure metric evaluates the maximum distance (d) needed to move the boundaries of the CT mask to completely cover the MRI mask [28].

$$\text{HD} = \max_{\text{CT}_r} \{ \min_{\text{MR}_r} \{ d(\text{CT}_r, \text{MR}_r) \} \}. \quad (7)$$

These metrics were calculated for four classes of the cortical bone, soft tissue, fat, and air cavity. The performance of the HSEG-based μ -map was illustrated in a joint histogram to determine the degree of similarity (in the form of correlation) between the MR and CT-based μ -maps and the sinograms of attenuation correction factor (ACF).

Results

Figure 2 represents the outcome of each step in the process of generating μ -maps for representative MR images. Figure 2a shows that the imaging technique produced a proper contrast between the desired classes (soft tissue, fat, and cortical bone-air) that increased the performance of SFCM as an intensity-based clustering approach. Figure 2b shows that inhomogeneity correction acceptably decreased the bias field on the MR images and improved clustering of data (Fig. 2c). It was observed that clustering cannot be performed by SFCM without such a correction. Figure 2d shows the μ -maps and the performance of HSEG for the separation of cortical bone, soft tissue, fat, internal air cavity, and external air segments. Visual inspection reveals the potential of the strategy for the segmentation of pelvic MR images.

The results of the two-step registration for the pelvic area as a non-rigid region are illustrated in Fig. 3. The cortical bone in the affine-transformed CT was a poor match with the corresponding cortical bone in the MR image (Fig. 3d, e). After the application of the B-spline transform, they showed a visually acceptable match (Fig. 3g, h) for use in evaluation. Similarly, the average of Dice ($92.1 \pm 5\%$) and Jaccard metrics ($94.4 \pm 3\%$) in the pelvic region indicate that the CT and MR images were acceptably matched together.

Figure 4 shows the μ -maps derived from the MRI and CT images in the coronal and transverse planes along with their different maps. Visual assessment confirms that the accuracy of the HSEG-based μ -map in the most regions was comparable to the CT-based μ -map except for the femoral head (Fig. 4, red arrows). The results of the assessment of HSEG using the sensitivity, Dice, Jaccard, and HD metrics are summarized in Table 1. The Dice,

sensitivity, and Jaccard metrics were greater than 72, 66, and 57 %, respectively, in all regions. The HD was less than 4.17 mm for cortical bone and internal air cavity. Table 2 shows the RVE data and the volumes of the segmented regions. The RVEs in the cortical bone, soft tissue, fat tissue, and air cavity regions were -31.7 ± 4.21 , 12.2 ± 6.14 , -23.8 ± 4.62 , and $26.9 \pm 17.22\%$, respectively. A negative RVE signifies the underestimation of the volume by HSEG.

Figure 5 shows the total joint histograms of the CT and HSEG-based μ -maps and the corresponding sinograms for 270 slices and complex slices. Visual assessment reveals the similarity between μ -maps in all regions with a slight deviation in μ of 0.10 cm^{-1} , as shown in Fig. 5a and c. Moreover, the correlation of all slices yielded the correlation coefficients of 0.993 ± 0.002 and 0.983 ± 0.017 , respectively, for μ -maps and ACF sinograms. The results for the more complicated slices were 0.991 ± 0.002 and 0.947 ± 0.003 , respectively, and for the less complex slices were 0.997 ± 0.002 and 0.994 ± 0.002 , respectively.

Discussion

In whole-body imaging, SEG-based strategies, such as the approaches used in commercial PET/MRI scanners, are faster and more robust for dealing with anatomical variation and non-rigidity than approaches based on AT and AT/PR [9, 16]. These strategies, such as the methods proposed by Martinez-Mollers et al. and Schulz et al., generate inaccurate μ -maps by ignoring cortical bones and underestimating the volume of internal air cavities [10, 11]. The method proposed by Martinez-Mollers et al. noticeably omitted internal air cavities while using a large morphologic closing filter (5 mm in each spatial direction) [5].

The present study considered cortical bones and internal air cavities in the μ -maps of the pelvic region using the algorithm illustrated in Fig. 1. The proposed algorithm consists of a dedicated imaging technique that increases the contrast between regions and the HSEG to classify MR images on the basis of intensity and morphologic characteristics. This technique takes the advantage of the SEG approach and specific features in bones (symmetry, similarity, area, and perimeter) to generate a five-class μ -map comprising fat, soft tissue, cortical bone, internal air cavity, and background. To our knowledge, this is the first study to consider cortical bones and air cavities in the μ -map of pelvic region using this technique.

The visual assessment of Fig. 2 and the results presented in Tables 1 and 2 reveal that SFCM acceptably enabled clustering of the fat and soft tissue on the dedicated MR images. For example, the values for evaluation metrics in soft tissues (Dice of $86 \pm 18\%$, sensitivity of $90 \pm 4\%$,

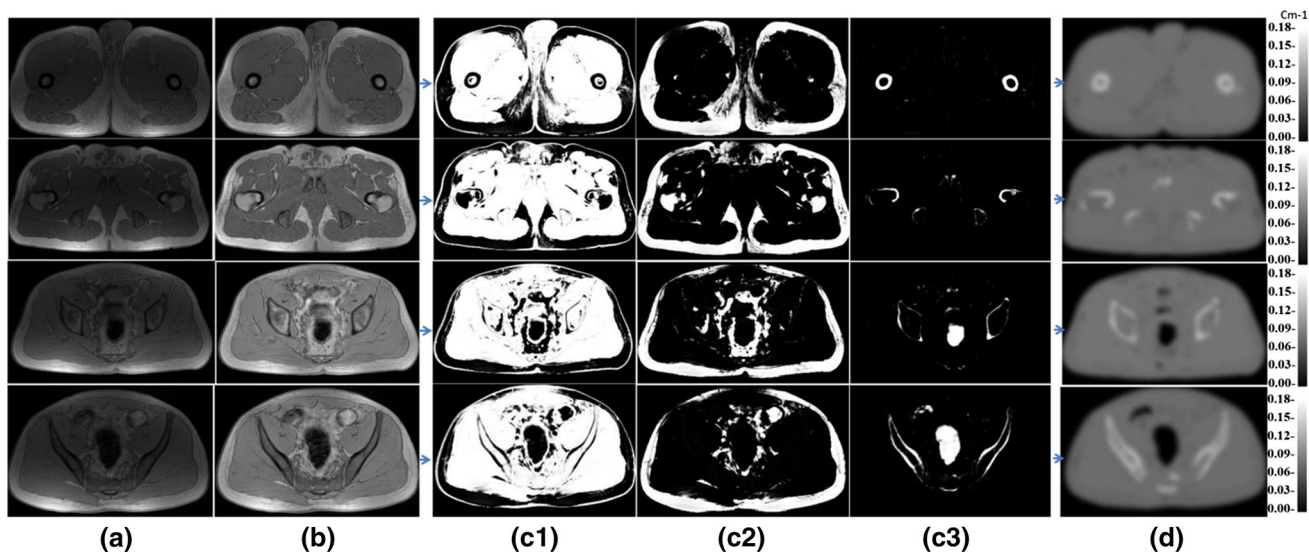


Fig. 2 Outcome of each step in the process of generating μ -maps for representative images. *a* MR images are provided by the STE pulse sequence, *b* bias field correction by Manjoun's approach, *c* the

clusters created by the SFCM approach; *c1* cluster soft tissue, *c2* cluster fat, *c3* cluster cortical bone-air cavity, *d* five-class μ -maps

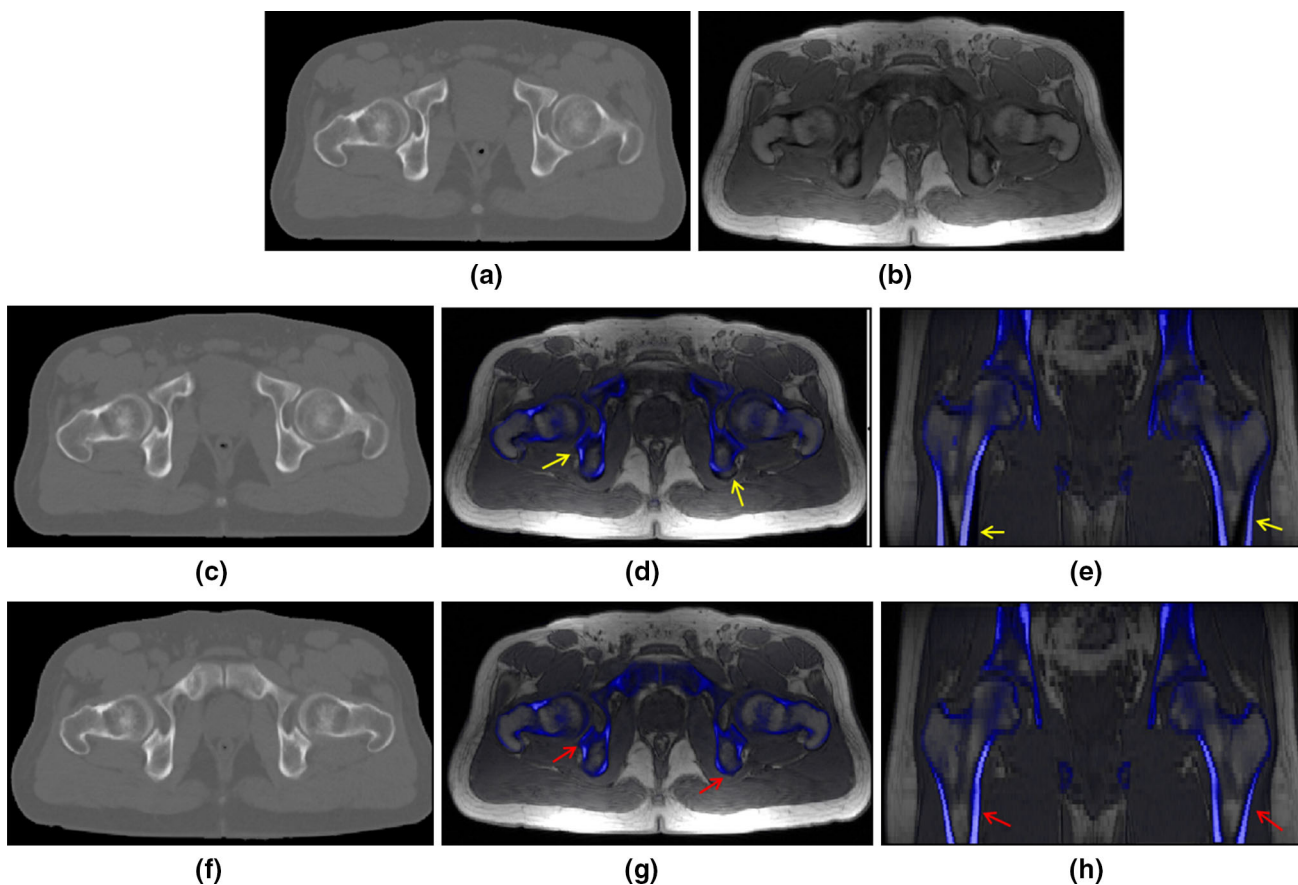


Fig. 3 Two-step registration approach for accurate matching the 3D-CT images to the 3D-MR images in pelvic region. *a* CT image, *b* MR image, and *c* affine-transformed CT; overlaying the bones in the affine-transformed CT on MRI *d* transverse view, *e* coronal view, and

f B-Spline transformed CT; overlaying the bones in the B-spline transformed CT on MRI *g* transverse view and *h* coronal view. *Yellow arrows* show wrong overlay in affine registration. *Red arrows* show acceptable overlay in B-spline registration

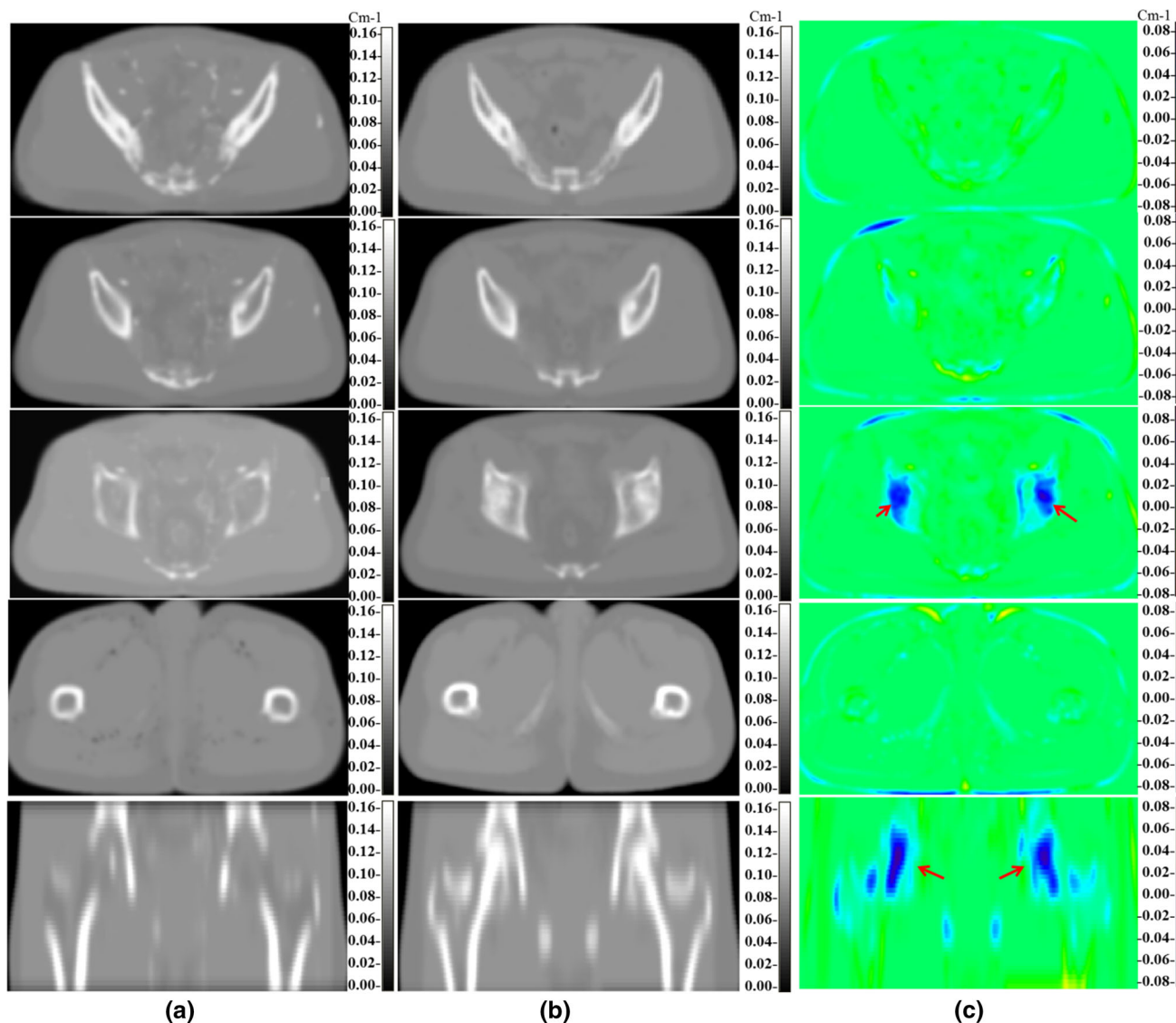


Fig. 4 **a** μ -maps generated from MR images using the HSEG method, **b** μ -maps generated from CT images, and **c** difference maps in coronal and transverse view. *Red arrows* show femoral head ignoring in the HSEG method

Table 1 Quantitative assessment of the HSEG-based segmentation procedure by voxelwise comparison

	Sensitivity (%) Mean \pm SD	Dice similarity (%)	Jaccard similarity (%)	Hausdorff distance (mm)
Cortical Bone	66 \pm 13	72 \pm 11	57 \pm 18	4.17 \pm 1.3
Internal Air	68 \pm 20	73 \pm 10	63 \pm 15	4.03 \pm 1.0
Soft tissue	90 \pm 4	86 \pm 18	77 \pm 6	6.6 \pm 1.5
Fat	70 \pm 11	77 \pm 25	65 \pm 22	4.66 \pm 2.4

The CT-based segmentation procedure is considered as reference

and HD of 6.6 ± 1.5 mm) and fat tissue (Dice metric of 77 ± 25 %, sensitivity of 70 ± 11 %, and HD of 4.66 ± 2.4 mm) verify this claim. The same trend was observed for the RVE index, for which the mis-registration is a confounder [29]. Table 2 shows the RVEs for segmented fat, and soft tissue were -23.8 ± 4.62 and

12.2 ± 6.14 %, respectively. These efficiently demonstrate the proposed method for segmenting the fat and soft tissues in pelvis. These results are important, because the separation of fat and soft tissue was achieved with only one image, whereas the protocol proposed by Martinez-Mollers et al. requires two images (in-phase and oppose-phase) [9].

Table 2 RVE of the regions segmented by the HSEG approach in comparison with the segmented CT as reference in all data set

Regions	Average number of pixels		Relative volume (%) Mean \pm SD
	Segmentation based on		
	HSEG	CT	
Cortical bone			
Femur	18,452	20,210	-8.7 ± 6.03
Femur head	1005	3406	-70.5 ± 8.03
Iliac and ilium	17,923	23,277	-23 ± 5.10
Cortical bone	66,799	97,802	-31.7 ± 4.21
Fat tissue	671,257	880,910	-23.8 ± 4.62
Soft tissue	1,864,813	1,662,024	12.2 ± 6.14
Internal Air	9431	7431	26.9 ± 17.22

Because the internal air cavities and cortical bones in MR images have similar intensities, they could not be separated by SFCM, which is an intensity-based segmentation method (Fig. 2c). Table 1 shows that the Dice, sensitivity, and Jaccard metrics for the cortical bones segmented using morphologic characteristics were 72 ± 11 , 66 ± 13 , and 57 ± 18 %, respectively. In comparison with these results, the Hofmann method [7], an AT-PR approach to segment cortical bones, yielded a sensitivity of 40 ± 0.15 %, Dice of 58 ± 0.09 %, and Jaccard of 35 ± 0.06 %. Cabello et al. [30] investigated UTE-based segmentation on head organs and reported that the Dice and Jaccard metrics were 69 and 53 %, respectively, for bone segmentation. Dice metrics of 65 % (53–69 %; Aasheim et al.), 75 ± 5 % (Juttukonda et al.), and 49 % (34–69 %; Delso et al.) have been reported that show similar outcomes for UTE-based segmentation [15, 31, 32]. The proposed method showed better results relative to the Hofmann approach and similar results relative to the UTE approach. Although this method presents fewer challenges in the pelvic region than the AT and UTE methods [9], it should be noted that the results of the current study were compared with UTE data for the head, because the results for UTE-based segmentation were reported only for head organs.

The proposed algorithm had difficulty extracting thin (less than a slice in thickness) cortical bone, such as of the femoral head (RVE of -70 ± 8 %) because of the partial volume effect, a common limitation in SEG-based strategies for MRAC (Fig. 4; Table 2) [5]. Recent studies by the authors and Samarin et al. found that this issue might have a slight influence on the accuracy of tracer uptake [12, 27]. Samarin et al. investigated the effect of cortical bone on the accuracy of tracer uptake and reported that thin cortical bones had a negligible effect (5 %) compared to thick cortical bones in the pelvic region (30 %) [12, 27].

Notable performance by the HSEG for internal air segmentation (Dice of 73 ± 10 %, sensitivity of 68 ± 20 %, Jaccard of 63 ± 0.15 %, and RVE of 26.9 ± 17.22 %) was achieved (Tables 1, 2; Fig. 2). Although the volume of air cavities is primarily ignored in the MRAC employed in the current PET/MRI systems, the above results show acceptable performance of the proposed strategy [5, 6, 9]. Because the pelvic region often contains massive air cavities (Fig. 2), substituting all or parts of the air cavity with soft tissue in μ -map will affect local uptake and also likely global uptake owing to reconstruction process [10, 11].

The joint histograms plotted in Fig. 5 indicate that the HSEG and CT-based μ -maps correlated well with average correlation coefficients of >0.981 . The abrupt deviation created at $\mu = 0.10 \text{ cm}^{-1}$ (Fig. 5a, c) arose from replacing μ of cortical bone with soft tissue, in particular for regions having thin cortical bone, such as the femoral head. To compensate for the lack of access to PET images, ACF sinograms were computed from μ -maps to evaluate the effect of the proposed μ -maps on PET reconstruction. The joint histograms and high correlation coefficients for the ACF maps suggest that they have a similar effect on reconstruction procedure for PET/MRI.

As mentioned, the SEG-based approaches used in commercial PET/MR systems ignore cortical bone and most air cavity volume [6, 9]. It is well known that a UTE sequence of the head generates artifacts in regions with a large FOV, such as the pelvis [14]. The AT-based segmentation approaches are time-consuming and error prone in non-rigid regions, such as the pelvis. It is reported that the magnitude of matching error in some non-rigid regions is even more than the cortical bone thickness [7, 33]. As such, they are less able to deal with organs, such as the bowel with movable and massive air cavities [14, 16]. It appears that the proposed approach is more suitable for the pelvic region, which is a common target of PET/MRI imaging.

The performance of this hybrid approach in bone structure with pathologic variations, e.g., metastatic bone or implants, could be problematic (similar to AT) and requires further study. The lack of access to PET/MRI systems for more comprehensive evaluation was the main limitation of the present study. Further investigation is underway to decrease concerns by increasing the optimization of the protocol, improving the accuracy of the registration procedure, and exploiting the optimized method for the entire body.

Conclusion

This work proposes a novel hybrid method for segmenting dedicated MR images into five classes for MRAC on PET/MRI systems. The results reveal that the proposed method

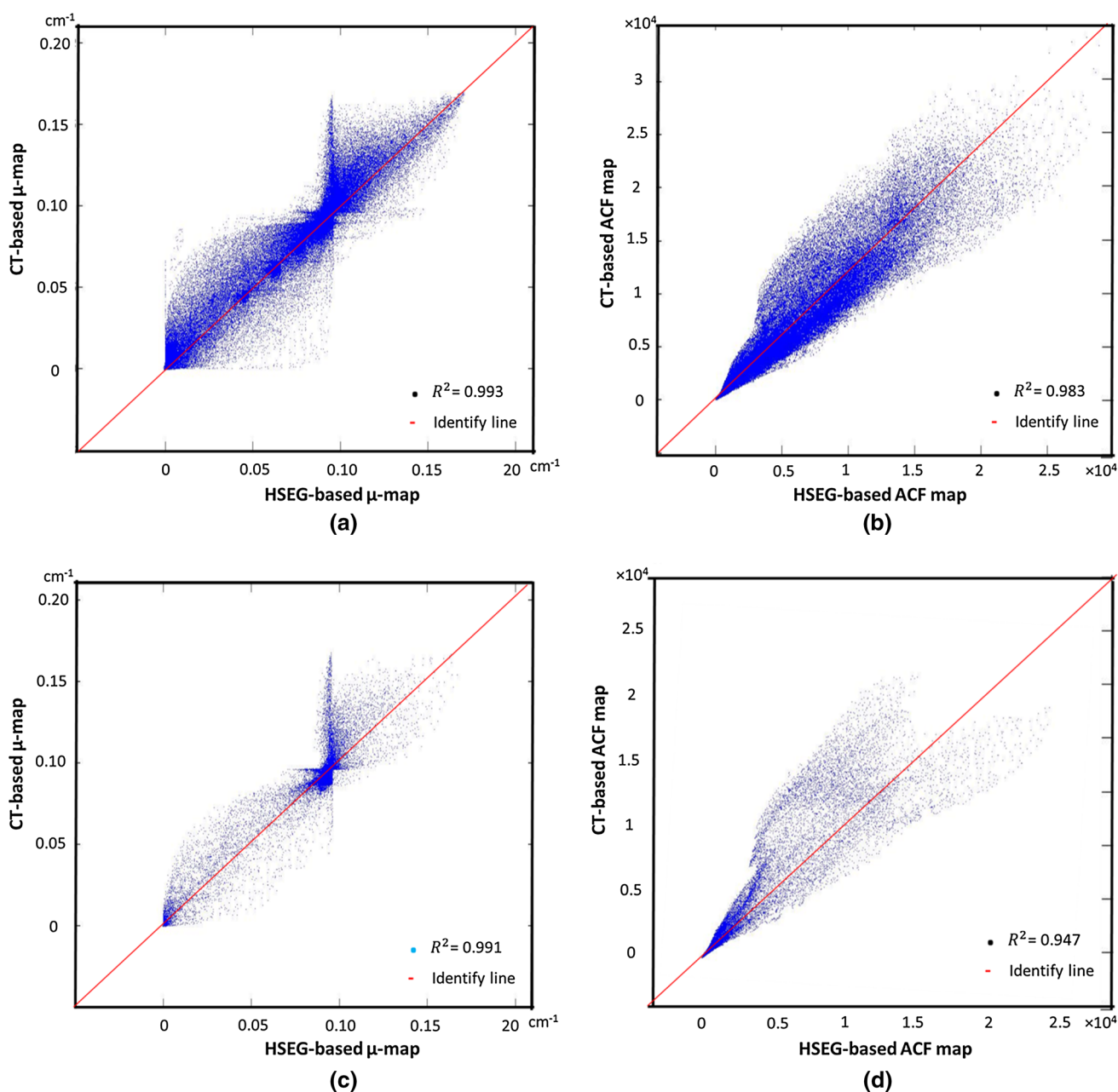


Fig. 5 Joint histograms of integrated μ -maps (a and b 270 slices) and integrated sinograms (c and d complicated slices)

can accurately segment cortical bone and air cavities in the pelvic region which are ignored in current PET/MRI systems. In addition, fat segmentation was acceptably performed using only one image, whereas two images are required in scanners. Cortical bone, internal and external air, soft tissue, and fat segmentation using an image provided by a conventional MR sequence reflect the novelty of our work. The suggested method can improve the accuracy of SUV estimation on PET/MRI imaging in clinical images.

Acknowledgments This work was supported under Grant Number 25095, Tehran University of Medical Sciences, Tehran, Iran.

Compliance with ethical standards

Conflict of interest The authors declare that they have no conflict of interest.

References

1. Disselhorst JA, Bezrukov I, Kolb A, Parl C, Pichler BJ. Principles of PET/MR imaging. *J Nucl Med.* 2014;55(Suppl 2):2S–10S.
2. Zaidi H, Del Guerra A. An outlook on future design of hybrid PET/MRI systems. *Med Phys.* 2011;38:5667–89.
3. Souvatzoglou M, Eiber M, Martinez-Moeller A, Fürst S, Holzapfel K, Maurer T, et al. PET/MR in prostate cancer: technical

- aspects and potential diagnostic value. *Eur J Nucl Med Mol Imaging*. 2013;40:79–88.
4. Bezrukov I, Mantlik F, Schmidt H, Schölkopf B, Pichler BJ. MR-based PET attenuation correction for PET/MR imaging. *Semin Nucl Med*. 2013;43:45–59.
 5. Martinez-Möller A, Souvatzoglou M, Delso G, Bundschuh RA, Chefd'hotel C, Ziegler SI, et al. Tissue classification as a potential approach for attenuation correction in whole-body PET/MRI: evaluation with PET/CT data. *J Nucl Med*. 2009;50:520–6.
 6. Schulz V, Torres-Espallardo I, Renisch S, Hu Z, Ojha N, Börnert P, et al. Automatic, three-segment, MR-based attenuation correction for whole-body PET/MR data. *Eur J Nucl Med Mol Imaging*. 2011;38:138–52.
 7. Hofmann M, Bezrukov I, Mantlik F, Aschoff P, Steinke F, Beyer T, et al. MRI-based attenuation correction for whole-body PET/MRI: quantitative evaluation of segmentation-and atlas-based methods. *J Nucl Med*. 2011;52:1392–9.
 8. Ay MR, Akbarzadeh A, Ahmadian A, Zaidi H. Classification of bones from MR images in torso PET-MR imaging using a statistical shape model. *Nucl Instrum Meth A*. 2014;734:196–200.
 9. Martinez-Möller A, Nekolla SG. Attenuation correction for PET/MR: problems, novel approaches and practical solutions. *Z Med Phys*. 2012;22:299–310.
 10. Keereman V, Van Holen R, Mollet P, Vandenberghe S. The effect of errors in segmented attenuation maps on PET quantification. *Med Phys*. 2011;38:6010–9.
 11. Akbarzadeh A, Ay MR, Ahmadian A, Alam NR, Zaidi H. MRI-guided attenuation correction in whole-body PET/MR: assessment of the effect of bone attenuation. *Ann Nucl Med*. 2013;27:152–62.
 12. Samarin A, Burger C, Wollenweber SD, Crook DW, Burger IA, Schmid DT, et al. PET/MR imaging of bone lesions—implications for PET quantification from imperfect attenuation correction. *Eur J Nucl Med Mol Imaging*. 2012;39:1154–60.
 13. Berker Y, Franke J, Salomon A, Palmowski M, Donker HC, Temur Y, et al. MRI-based attenuation correction for hybrid PET/MRI systems: a 4-class tissue segmentation technique using a combined ultrashort-echo-time/Dixon MRI sequence. *J Nucl Med*. 2012;53:796–804.
 14. Boellaard R, Quick HH. Current image acquisition options in PET/MR. *Semin Nucl Med*. 2015;45:192–200.
 15. Delso G, Carl M, Wiesinger F, Sacolick L, Porto M, Hüllner M, et al. Anatomic evaluation of 3-dimensional ultrashort-echo-time bone maps for PET/MR attenuation correction. *J Nucl Med*. 2014;55:780–5.
 16. Keereman V, Mollet P, Berker Y, Schulz V, Vandenberghe S. Challenges and current methods for attenuation correction in PET/MR. *Magn Reson Mater Phys*. 2013;26:81–98.
 17. Khateri P, Rad HS, Fathi A, Ay MR. Generation of attenuation map for MR-based attenuation correction of PET data in the head area employing 3D short echo time MR imaging. *Nucl Instrum Meth A*. 2013;702:133–6.
 18. Manjón JV, Lull JJ, Carbonell-Caballero J, García-Martí G, Martí-Bonmatí L, Robles M. A nonparametric MRI inhomogeneity correction method. *Med Image Anal*. 2007;11(4):336–45.
 19. Chuang K-S, Tzeng H-L, Chen S, Wu J, Chen T-J. Fuzzy c-means clustering with spatial information for image segmentation. *Comput Med Imaging Graph*. 2006;30:9–15.
 20. Russ JC. *The image processing handbook*. CRC press; 2015.
 21. Serra J. Morphological filtering: an overview. *Sig Process*. 1994;38(1):3–11.
 22. Khateri P, Rad HS, Jafari AH, Kazerooni AF, Akbarzadeh A, Moghadam MS, et al. Generation of a four-class attenuation map for MRI-based attenuation correction of PET data in the head area using a novel combination of STE/Dixon-MRI and FCM clustering. *Mol Imaging and Biol*. 2015; 1–9.
 23. Chan TF, Vese LA. Active contour and segmentation models using geometric PDE's for medical imaging. *Geometric methods in bio-medical image processing*. USA: Springer; 2002. p. 63–75.
 24. ICRU. International commission on radiation units and measurements. Report no. 44; 1989.
 25. Mairal J, Bach F, Ponce J, Sapiro G, Zisserman A, editors. Non-local sparse models for image restoration. In: 2009 IEEE 12th International Conference on Computer Vision. pp. 2272–2279.
 26. Klein S, Staring M, Murphy K, Viergever M, Pluim JP. Elastix: a toolbox for intensity-based medical image registration. *IEEE Trans Med Imaging*. 2010;29:196–205.
 27. Akbarzadeh A, Gutierrez D, Baskin A, Ay MR, Ahmadian A, Alam NR, et al. Evaluation of whole-body MR to CT deformable image registration. *J Appl Clin Med Phys*. 2013; 14.
 28. Crum WR, Camara O, Hill DL. Generalized overlap measures for evaluation and validation in medical image analysis. *IEEE Trans Med Imaging*. 2006;25:1451–61.
 29. Fleiss JL, Levin B, Paik MC. *Statistical methods for rates and proportions*. Wiley; 2013.
 30. Cabello J, Lukas M, Förster S, Pyka T, Nekolla SG, Ziegler SI. MR-based attenuation correction using ultrashort-echo-time pulse sequences in dementia patients. *J Nucl Med*. 2015;56:423–9.
 31. Aasheim LB, Karlberg A, Goa PE, Håberg A, Sørhaug S, Fagerli U-M, et al. PET/MR brain imaging: evaluation of clinical UTE-based attenuation correction. *Eur J Nucl Med Mol Imaging*. 2015; 1–8.
 32. Juttukonda MR, Mersereau BG, Chen Y, Su Y, Rubin BG, Benzinger TL, et al. MR-based attenuation correction for PET/MRI neurological studies with continuous-valued attenuation coefficients for bone through a conversion from R2* to CT-Hounsfield units. *NeuroImage*. 2015;112:160–8.
 33. Arabi H, Zaidi H. Magnetic resonance imaging-guided attenuation correction in whole-body PET/MRI using a sorted atlas approach. *Med Image Anal*. 2016;31:1–15.